Sensing the Frictional State of a Robotic Skin via Subtractive Color Mixing

Xi Lin and Michaël Wiertlewski *Member, IEEE*

***Abstract*—The perception of surface properties such as shape and slipperiness is crucial to ensure that the hand-held object is stable. Without touch, precise manipulation becomes difficult. Some robotic tactile sensors use cameras that observe the elastic deformation of a membrane to detect edges or slippage of the contact. The perception of the contact state drove innovative control strategies. However, previous methods on these lines do not include quantitative means of measuring the 3-dimensional deformation of the skin or suffer from a lack of spatial resolution. Here we present a tactile sensor based on a subtractive color mixing process designed to track the 3-dimensional displacement of an array of markers, using the information delivered by the color channel of off-the-shelf cameras. The distributed shear and normal deformation can be assessed from the spectrum of the light reflected and refracted by an array of diffusive and transmissive markers placed on two superimposed layers. The markers show various blends of colors, depending on the displacement at the surface. The color pattern of each marker can be tracked with little computation and remains robust to external lighting. The ability to sense the 3-dimensional deformation field can improve robotic perception of frictional properties which have applications in the fields of robotic control and human-robot interactions.**

***Index Terms*—Force and Tactile Sensing; Soft Material Robotics**

I. Introduction

FOR both robots and humans, tactile perception is essential to be able to learn and perform appropriate hand gestures for grasping and manipulating objects [1]. In particular, humans' tactile perception of the state of contact between a finger and an object generates information on which the stability of the grasp depends [2]. The object might have to be moved reliably from one place to another without inducing any perception of relative motion with respect to the fingers. In other scenarios, the opposite problem might arise when the object has to be slid to a certain part of the hand in order to be properly lifted. These chains of events involve fine and dexterous control of the frictional contact between the object and the skin. In humans, the state of friction is thought to be assessed not by directly determining the normal and tangential components of the force, but rather depending on which part of the fingertip is stuck to the object and which part is starting to slide [3], [4].

Manuscript received: September, 10, 2018; Revised December, 3, 2018; Accepted December, 29, 2018.

This paper was recommended for publication by Editor Allison Okamura upon evaluation of the Associate Editor and Reviewers' comments. This work was supported by ANR under grant 16-CE10-0003

[1]Xi Lin and Michaël Wiertlewski are with Aix-Marseille University, CNRS, ISM, 13009 Marseille France. xi.lin@univ-amu.fr, michael.wiertlewski@univ-amu.fr

Digital Object Identifier (DOI): see top of this page.

The contribution of tactile sensing to grasping and manipulation has been well recognized [5]. Artificial skin based on piezo-resistive [6], piezoelectric [7], electrostatic [8], [9], optical [10] and even ultrasonic transducers [11] have been previously tested. These tactile sensors convert the localized deformation of the surface into a signal that is stored and interpreted by a computer. These sensors can collect information that is not accessible visually, not only because the contact is often hidden from view, but mostly because the information about the contact, such as the slipperiness of the surface or the compliance of the material, requires mechanical interactions to be revealed.

Many of the latest methods designed for this purpose focus on measuring the pressure field applied normal to the surface, which suffices to recognize objects [12]. It has been established, however, that the lateral traction produced by friction is essential to control robotic grippers [13], [14]. A dense array of sensors also requires a cumbersome set of electrical interconnections and conditioning electronics when a large number of transducers are used.

Some sensors use a camera to transduce the deformation of an elastic body or membrane [15], [16], [17], [18]. The usual procedure starts by locating the center of black or white markers. The lateral motion of each marker can be easily determined with computer-vision algorithms and the distributed measurements are sufficiently rich to recognize the nature and orientation of an object. However, these methods do not directly provide the normal and lateral pressure field at the interface. In particular, the local friction coefficient, expressed by the ratio between the lateral shear stress and the normal stress cannot be directly observed although this parameter is essential for characterizing the adherence of an object and its stability in the hand.

To address these challenges, we developed the camera-based sensor, shown in Fig. 1a and 1b, which not only tracks the lateral motion of an array of markers but also resolves the motion normal to the surface. The sensor recruits a double array of overlapping semi-transparent colored markers. The deformation of the markers, which are attached to the interaction surface, affects their shape and their color content, which makes it possible to reconstruct the 3-dimensional deformation field at the interface.

II. Background on camera-based robotic fingertip

Since cameras are ubiquitous and provide a fast, reliable way of transferring real-time data to a controller, many artificial fingertips have included an off-the-shelf optical sensor, thus reducing the need for the custom-made electronics required in piezoresistive or capacitive sensor arrays.

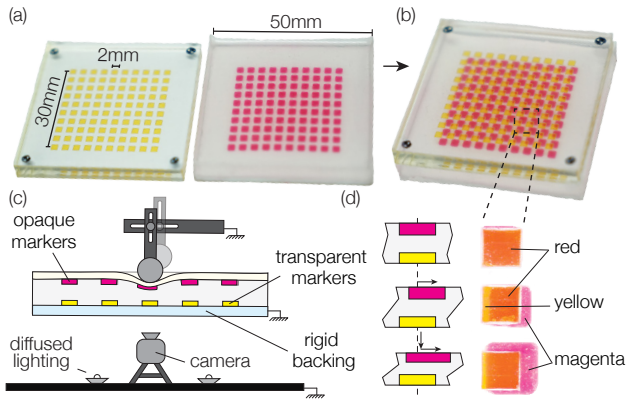

Fig. 1. (a) Exploded view of the tactile sensor based on color mixing. Yellow markers are rigid and magenta markers are deformable. (b) View of the sensor assembly. (c) Diagrams illustrating the deformation of each layer under an inclined external force. (d) Compressive and shear deformations can readily be determined from the color pattern.

Artificial fingertips are often made by including in a soft hemispheric membrane markers that can easily be tracked using state-of-the-art image segmentation methods. Once the membranes elasticity and shape have been determined, the stress at the surface can be calculated by performing least-squares regressions [15]. Markers can be mounted on pillars to amplify the rotation of the membrane and improve the sensitivity of these sensors to edges [19], [16]. In these devices, the sensor encodes a 2-dimensional displacement field in which the local traction and the indentation are combined.

The GelForce sensor includes two layers of spherical markers of different colors to determine the full 3-dimensional stress field. Any stresses imposed on the surface will induce deformations of the solid, the intensity of which depends inversely on the depth of the markers. By performing a linear interpolation, it is possible to determine the lateral and normal stresses from the displacement of markers located at different depth [20]. The efficiency of this method has been established with an artificial finger equipped with a 5x5 grid [17]. However, as these markers are opaque, only a few markers can be seen at the same time, which reduces the spatial resolution of the system. In another interesting approach is based on the apparent sharpness of the marker when it moves out of focus [21]. The Gelsight sensor provides a picture of the deformation field using photogrammetric methods [18]. This sensor is composed of a thin layer of silver flakes, which diffuse light in all directions. The relief of an object that is touched can be reconstructed using three separate illumination sources and a Lambertian reflectance model. This setup gives the shape of the object with an unmatched level of precision, and hence the relative position of a tactile feature [22]. However, since the motion of artificial skin particles is not tracked, the stress field at the interface cannot be easily determined. The authors solved this problem by adding a layer of dots giving information about slippages [23].

Our own method focuses on uniformly sampling the deformation field at the surface of an elastic body. With this marker-based method, the shear deformation is determined via the centroid tracking of each marker, and the normal deformation, via the blend of colors between two layers of markers acting as a band-limited optical filter.

III. Sensor principle and manufacturing

A. Design rationale

The main purpose of this tactile sensor is to assess the spatiotemporal changes in the frictional state at the point of contact between the skin of the finger and the object touched. In order to ensure that the sensor collects meaningful information, we looked at how human fingertips sense shapes and the state of friction. This yielded the following requirements:

1) The sensor must be able to detect surface undulations which are at least 10 times smaller than the contact area. Without any relative motion, surface defects as small as 1 mm in a ≈10 mm-diameter contact area can be detected by human touch alone [24].
2) Friction plays a crucial role in the stability of our grasp [25] and in the perception of materials [26]. Because of this, the shear and normal components of the deformation field have to be determined.
3) The elasticity of the medium diffuses the stress throughout the solid so the deeper the markers are located, the more individual motion are smoothed out. To avoid this, the markers should be located less than 0.5 mm from the surface [27].

One of the consequences of having a large number of markers is that each individual marker occupies only a few pixels and changes of size and location are hardy perceivable. Our approach overcomes this issue by making use of the color channels of cameras. Instead of finding the normal motion from the change in size of a pixellated monochromatic shape, our sensor encodes the normal motion reliably via a change of color, even when only a handful of pixels are used.

B. Color mixing from partial occlusion

The new sensor is constructed around a soft transparent silicone body in which two separate layers of colored markers are embedded. Markers closer to the surface of the skin are soft and reflect magenta light (that has a spectrum containing both blue and red wavelengths). In the implementation shown in Fig.1a, the setup is comprised of one hundred 2mm-wide markers placed 1mm apart. The second layer of markers overlaying the magenta marker array consists of a material that is transparent to light with a wavelength greater than 500 nm. The high-pass filter gave these markers a yellow appearance to the naked eye and to camera sensors. When pressure is applied to the surface of the sensor, the magenta markers are brought closer to the yellow filter, see Fig.1c. Shear forces will shift the center of each marker relative to each another. The combination of stretch, compression, and lateral shift creates a colored pattern, which specifies the direction and the magnitude of the displacement vector of the surface above the markers Fig.1d.

Fig. 2a and 2b are typical views of the two layers, showing the three colors magenta (which is white without any green), yellow (which is white without any blue) and red (which is

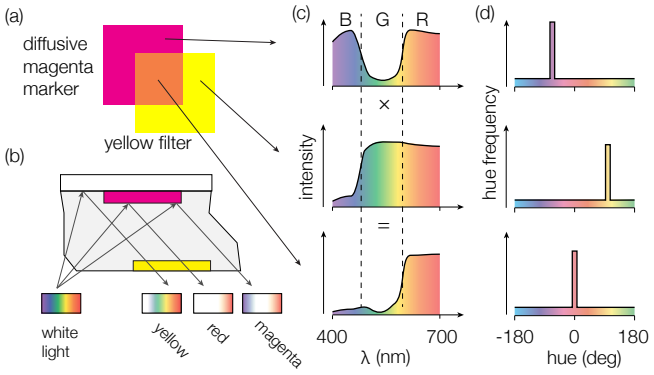

Fig. 2. (a) Diagram of the image of the marker observed by the camera. (b) The white light is scattered by either the background or the magenta marker. Some of the scattered light crosses through the yellow filter, which further filters the color spectrum. (c) Color spectra of the light after the reflection by the magenta markers, of the light after being transmitted trough the yellow markers, and of the light which is both scattered by the magenta markers and filtered by the transparent yellow filter. (d) Corresponding histograms of the hue channel in the HSV colorspace.

white any green or blue). Marker arrays are flooded with diffuse white light, which can be either diffused by the magenta markers or the white layer and possibly filtered by the yellow markers on its way back to the camera. All four combinations of the color spectrum shown in Fig. 2b can be seen in the resulting image. Physically, shifting from white to red occurs when the magenta markers reflect only the red and the blue parts of the spectrum and the blue is filtered out by the yellow layer, as described in Fig. 2c.

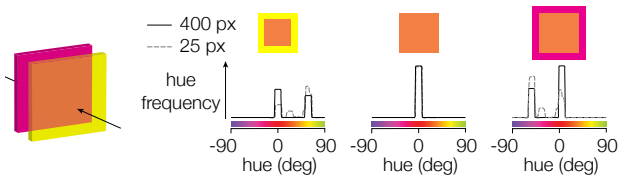

Fig. 3. Effect of the change in the size of the magenta markers on the histogram of the hue channel. The histogram is only slightly affected by the number of pixels in the image.

Humans and cameras alike detect only three bands in the optical spectrum, in the blue (≈450nm), green (≈580nm) and red (≈690nm) ranges. Images detected in the Red-Green-Blue color space can be converted into Hue-Saturation-Value (HSV) color space, where the value and the saturation depend only on the illumination of the markers and the hue channel contains the color information. An example of the hue intensity of typical light rays is presented in Fig. 2d. The hue channel is presented in the form of a color , where the colors are shown at an angle with respect to an arbitrary origin, set at red. In the HSV color space, the center of mass of the histogram of the hue channel depends on the normal displacement of the soft marker with respect to the transparent marker, see Fig. 3. Since changes in the hue of the image involve a large number of pixels carrying 24 bits of information (versus 1 bit in the case of segmented black and white images), these fluctation will be theoretically more visible in the case of small displacements than the apparent change in the marker size, which translates into greater sensitivity to the motion normal to the surface.

C. The opto-mechanical model

This section describes models for the optical and mechanical components of the complete sensor.

1) Effects of the focal length on the resolution: The reliability of the measurements depends on the camera and lens used to detect the markers. A longer telephoto lens will reduce the apparent changes in the marker size, and a simple model shows that the shorter the focal length, the more pronounced the motion of the moving marker will be.

The model illustrated in the Fig. 4a is based on the well-known pinhole camera model, in which light rays reflected by objects and reaching the image plane cross a point located one focal length from the image sensor.

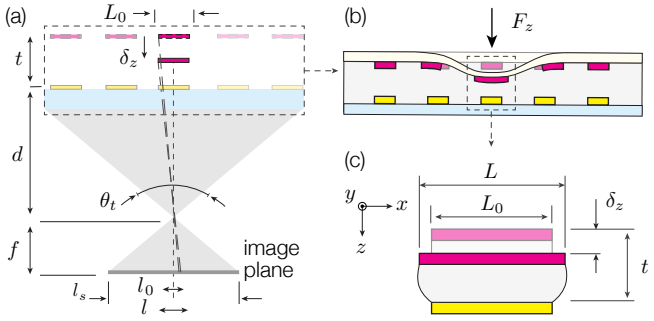

Fig. 4. (a) The pinhole camera model explaining how sensor motion is correlated to changes in apparent size. (b) The large Poisson coefficient of soft material results in significant stretching of the soft marker, which increases the signal to noise ratio. (c) The optimum thickness maximizing the apparent change in the case of a given external force is presented here, depending on the camera's angle of view.

The problem is constrained by the fact that n markers have to fit into the field of view θ. Each of the markers therefore has to cover a fraction of the field of view, $L_0/(d+t) = \tan(\theta/n)$. The pinhole model states that the angular size of the markers is the same on both sides of the focal point, $\tan(\theta/n) = l_0/f$. With these constraints in mind, maximizing the sensitivity of the sensor in the normal direction amounts to maximizing the relative changes in the apparent size $(l - l_0)/l_0$ with a given normal displacement of the marker δ_z. Let us take Thales' intercept theorem:

$$\frac{l}{f} = \frac{L_0}{d+t-\delta_z} \quad \text{and} \quad \frac{l_0}{f} = \frac{L_0}{d+t} \tag{1}$$

Combining these equations leads to the relative change:

$$\frac{l-l_0}{l_0} = \left(1 - \frac{\delta_z}{d+t}\right)^{-1} - 1 = \frac{\delta_z}{d+t} + O\left(\delta_z^2\right) \tag{2}$$

The result of this equation is shown in Fig. 5a. The smaller the distance to the object is, the more noticeable the changes will be. Smaller focal length optics are therefore preferred.

2) Mechanics and optimal thickness between layers: The top layer of the assembly is soft and the magenta markers can be stretched elastically. Stretching increases the actual size of the marker and therefore further enhances the sensitivity, see Fig. 4b.

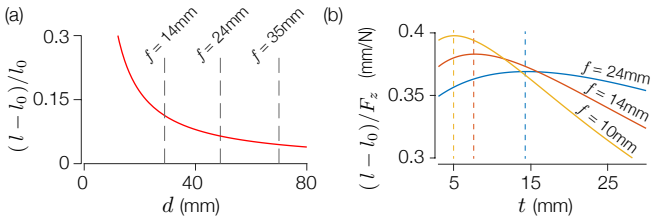

Fig. 5. (a) The soft magenta layer is pushed down towards the yellow filter. (b) The model predicts that a wide angle lens will give greater magnification at a given normal displacement of the marker.

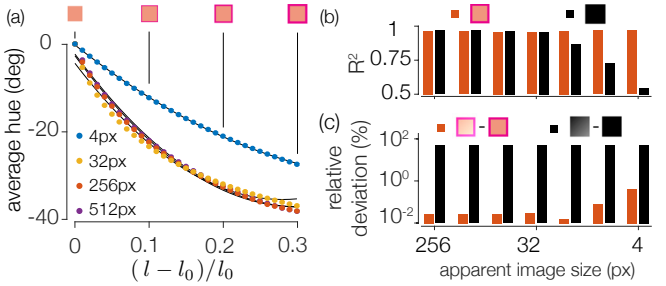

Fig. 6. (a) The hue measurements of the marker are almost insensitive to the apparent size. The simulation showed that the mean hue shifts smoothly towards the hue of the flexible magenta marker. (b) Effects of the apparent size on the accuracy of the polynomial fit. (c) Effects of the non-uniform luminosity on the displacement measurements.

A simple model for the deformation of the marker can be drawn up, taking in consideration only the elasticity of the material sandwiched between the two layers. In this simplified model, which is presented in Fig. 4c, the behavior of the material boils down to a compression ratio that can be described by the materials Young's modulus E, the thickness t and the marker size L, as well as a lateral extension corresponding to the Poisson's ratio ν. The compressive elasticity of the material just below the marker can be obtained by deriving Hooke's and Poisson's laws:

$$\delta_z = \frac{F_z}{EL_0^2}\,t \qquad \text{and} \qquad L = L_0\left(1+\nu\frac{\delta_z}{t}\right) \tag{3}$$

We can see that a thicker sensor gives greater marker mobility at a given external force, at the expense of a smaller change in the apparent area. A thickness that maximized the compliance while keeping a large stretch was obtained by combining equations 1 and 3. Assuming that we have a Young's modulus of $E = 0.4$ MPa, Poisson's ration $\nu = 0.5$ and a marker size of $L_0 = 2$ mm projecting an image onto a $l_s = 35$ mm sensor, the results obtained with three different lenses are presented in Fig. 5b. The model argues in favor of a soft material with a low Young's modulus, which could be thin and deformable.

D. Robustness to pixel density and lighting conditions

One of the main advantages of using color channels is that the markers configuration can be sorted out using just a few pixels. A simulation was run to verify the robustness of the method when only a few pixels were used. A single marker was first drawn using a vector graphics editor (Illustrator, Adobe, San Jose, CA, USA) to depict an opaque magenta marker underlying a yellow marker with an opacity of 50%. The size of the magenta marker was changed to provide a range of artificial normal displacements. Images were rasterized in a 512x512 image and a pyramid gaussian process was used to create smaller versions, with the goal to emulate the effect of having smaller markers. Once the small version was created, an anti-aliasing filter that leverages a Gaussian filter with standard deviation set to 1/8th of the size of the image was added to remove artifacts.

Fig. 6a shows that even with a apparent size of 4x4 pixels, displacements can be satisfactorily approximated by a second order polynomial fit ($R^2 > 0.98$). We also ran simulations on the effects of changing the pixel density on the estimated size of black and white markers. Fig. 6b shows the dramatic effects of decreasing pixel density on the black and white markers, resulting in a steady decrease in the accuracy of the polynomial fit, which goodness of fit reach as low as $R^2 = 0.5$ when the apparent size is 4x4 pixels, while the hue-based method is only slightly affected.

Lastly, in order to gauge the robustness to illumination non-uniformity, we looked at the effect of adding a 25%-opacity gradient overlay. Fig. 6c reports the difference value of the hue or luminosity for the color-mixing and the black and white method respectively, between the non-uniform and the uniform illumination, relative to the overall range of measurement. This metric compares both methods using a dimensionless number. The results show that the accuracy of the color-based method decreased by less than 1% under non-uniform illumination, whereas the black and white markers have relative error as high as 50%.

E. Methods & Manufacturing

Because it relies only on color and transparency, the sensor can be constructed with inexpensive equipment and materials. The procedure used to make the two layers is presented in Fig. 7. First, a soft white compound (SortaClear 12 with Pigment Ignite, Smooth-On, Macungie, PA, USA) is poured into a 3-D printed mould (TPU95A, Ultimaker, Geldermalsen, Netherlands) to form the outer layer of the sensor. The soft material has a Young's modulus of $E = 0.4$ Mpa and a Poisson's ratio of $\nu = 0.5$. The white color serves to block out the light from the outside, while at the same time diffusing the white illumination. Once the outside layer has been cured, a rigid mask is set in place and a mixture of the same soft compound and a magenta dye is screen printed and heat-cured. A transparent layer (SortaClear 12, Smooth-On, Macungie, PA, USA) is cast on top of the magenta markers to fill the holes left by the mask. The transparent layer also protects the markers and sets the right thickness for the sensor, depending on the intended design. All the elastomer compounds are first degassed in a vacuum chamber before being poured into the mold. The rigid base is constructed by bonding a transparent yellow film (Color 410e, Luminis-Films, Peronnas, France) to a transparent acrylic substrate. The squares are cut by laser and the excess film is removed by hand. Lastly, the rigid and soft layers are bonded.

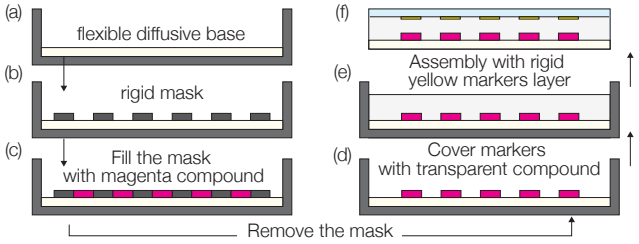

Fig. 7. The production process. (a) A white light-diffusive soft layer is placed in a cast. (b) Once it has been cured, a rigid mask is applied, and (c), the magenta markers are screen printed. (d) After the curing process, the mask is removed and the remaining markers are covered with a transparent compound. (e) The soft part is mounted on the rigid backing support.

The entire process can be performed within 3 days, including the curing. The cost of the raw material is about 4.5 euros in the case of this specific configuration and the process involves only commonly used manufacturing techniques.

IV. Experimental Results

A. Experimental Apparatus

Experiments were conducted on a laboratory test bench, a diagram of which is shown in Fig. 1c. The soft sensor was fitted into a stack of transparent laser-cut acrylic plates leaving only the top surface accessible for stimulation. Light was provided by 3 LED strips (Neutral White, RS Pro, Corby, UK) mounted on the side of the acrylic support. The light was diffused by the white layer to minimized the presence of any colored shadows and increased the color saturation. A manually adjustable 3-axis translation stage moved a probe with a swappable tip to apply normal and lateral deformation loads to the surface of the sensor. A high-resolution camera (A7Rii, Sony Corp., Tokyo, Japan) equipped with a zoom lens (24-70mm FE Zeiss, Sony Corp., Tokyo, Japan) set at a focal length of 24mm took high-resolution images of the markers with an aperture of $f/4$ and a locked white balance. With this setup, the deviation of the hue of 50 identical images was as low as 0.3 degree.

B. Marker tracking method

The image processing was performed using Matlab (Mathworks Inc, Natick, USA). The raw images were corrected to even out the nonuniform lighting using a morphological *tophat* filter, and the contrast was then enhanced using histogram equalization methods. The locations of the markers were segmented and labeled using the centroid detection method *regionprops*. At this stage, the location of each marker in the image plane is determined. In order to assess the normal motion, the image is segmented into regions of interest around each marker. Each region of interest was transformed in the HSV colorspace using *rgb2hsv*. The hue of each pixel which level of saturation was above 50%, ensuring that white pixel were excluded, was averaged to produce the estimation of the mean hue.

C. Single marker calibration

The behavior of one marker was modeled from the displacement data recorded when it was subjected to a 3-dimensional localized external load. The model was then inverted to estimate the displacement field in the case of more complex load distribution, using the superposition principle.

In this experiment, the indenter was a 4 mm diameter sphere, matching the resolution of the marker grid. The normal displacement is correlated with the hue of the marker and the lateral displacement is determined by tracking the centroid of each marker.

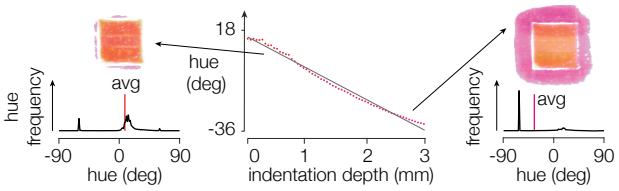

Fig. 8. Direct measurements show the linear relationship between the mean hue degree and the normal displacement of the surface.

To determined the effect of a normal displacement, the indenter was lowered onto the surface and an image was taken every 50 microns step over a 3 mm displacement. The results can be found in Fig. 8. The average hue is satisfactorily approximated by a linear trend ($R^2 = 0.99$).

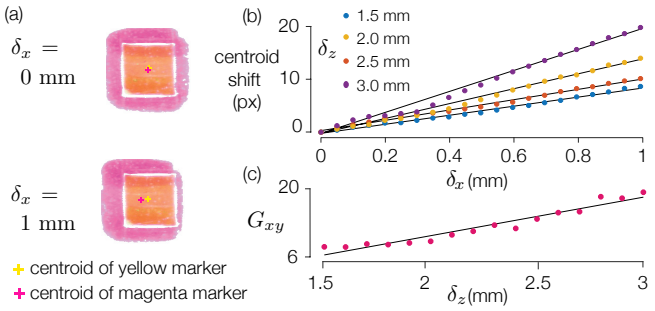

Fig. 9. The direct measurement confirms the linear relationship between the position of the centroid of the magenta marker and the displacement of the surface.

The changes in the position of the centroid of each marker also obeyed a linear relationship with the lateral displacement, see Fig. 9a. The lateral displacements were applied with a step size of 0.05 mm during a total displacement of 1 mm on the x axis. 15 series of lateral displacements were made by varying the normal indentation depth from 1.5 mm to 3 mm in 0.1 mm steps. By calculating the movement of the centroid of the soft marker under pressure loading, the linear relationships between the lateral displacement and the position of the centroid were determined for all 15 series of lateral movements with various normal indentation depths, as shown in Fig. 9b. Since the area of the magenta marker is more visible when the normal displacement is large, the relationship between the lateral displacement and the motion of the centroid G_{xy} was affected by the normal displacement applied to the surface. The value of the linear regression G_{xy} was found to be linearly correlated ($R^2 = 0.93$) with the normal displacement of the surface, see Fig. 9c.

The corresponding behavioral model can be summarized by the following set of equations :

$$h = G_z\,\delta_z + h_0 \quad \text{and} \quad c_{xy} = G_{xy}\,\delta_{xy} = (a\delta_z + b)\,\delta_{xy} \quad (4)$$

where G_z is the slope of the hue-normal displacement function, h is the hue value and h_0 the hue of the marker at rest. The gain G_{xy} between the displacement of the centroid c_{xy} and the displacement of the surface δ_{xy} is modeled by an affine relationship with a slope a and an intercept b.

D. Calibration validation

Once the behavior of a single marker had been measured, we inverted the model to make predictions based on the data recorded. Three series of lateral displacements were applied with normal indentation of 2, 2.5 and 3 mm. At each step, the indenter pushed the marker along the x and y axes simultaneously in 0.1 mm steps. The calibration process used was specific to the camera and sensor setup.The inversion of the model starts by finding the average before determining the normal displacement of the surface. Once this has been done, the appropriate scaling factor is used to determine the actual lateral displacement as a function of the distance.

$$\begin{cases} \delta_z = (h - h_0)/G_z \\ \delta_{xy} = c_{xy}/(a\delta_z + b) \end{cases} \quad (5)$$

Linear regression of the curves showed a good fit $R^2 > 0.94$ under all the conditions tested. The errors between the estimated $\hat{\delta}$ and actual displacements were less than $350\mu m$, which can be improved by using a non-linear approximation.

E. Reconstruction of the displacement field

The inverse model was then applied to the entire grid of markers. The effects of the parallax imposed on the corner markers were small and not compensated for. Some examples of the entire scene can be found in Fig. 10. With the flat indenter, Fig. 10a and 10b, the maximum deformation occurred on the edge of the shape, in line with the theory of contact mechanics [28]. Likewise, the normal displacement induced by the spherical indenter shown in Fig. 10c was in line with the parabolic distribution predicted by Hertz's contact theory. Interestingly, the lateral deformation of the surface was also visible because of the large Poisson's ratio the of elastomeric skin. This lateral radially distributed field, which contains information about the frictional state of both objects in contact, has been used in several robotic applications [29] and is thought to be involved in the perception of adherence in human tactile perception processes [2].

V. Conclusion and Limitations

We introduce a new approach to measure 3-dimensional displacement field with a color-based tactile sensor. The fastidious process of encoding the normal displacement is achieved by using the color channels, allowing to capture both the normal and lateral displacement of an array of colored markers based on the color pattern produced when transmitted through a reference translucent array. The sensor boast a precision that corresponds to 2% of the original size.

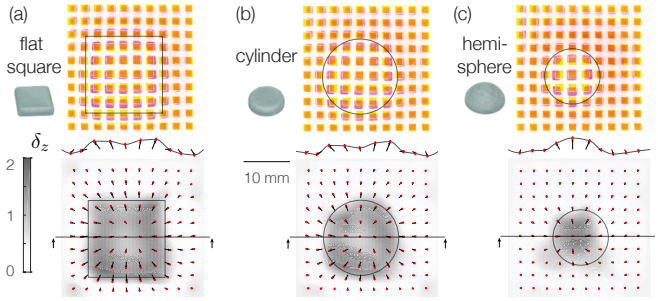

Fig. 10. Experiment with a square (a), a cylindrical (b) and hemispherical (c) probe. The normal distribution is in line within the literature and the direction of the deformation vector hints at the work of friction.

The design principles and experimental results show that this sensor is suitable for gauging the distributed 3-dimensional motion of a surface to which complex stress field involving friction are applied. However, suitable means of measuring the force applied to the surface still remain to be developed. A localized force applied at the center of the sensor will induce a displacement which has visible effects on every markers and deconvolution methods [7] can be used to determine the stress and traction forces exerted at the surface from the markers data. Besides the absence of force measurements, one limitation of the sensor is that the center of a marker that experiences a pure tilt will be measured with a systematic error. Spherical markers can limit this effect.

Finding means of measuring the distributed 3-dimensional interactions occur in the contact area between a surface and an external object is key to determine the properties of the material such as its compliance or shape, along with the dynamics of the contact, especially the occurrence of any incipient slippage. Tactile sensors have been found to be of great benefit in the field of robotic surgery [30], soft-object picking [31] and protheses [32].

VI. Future Work

Further investigations will focus on reconstructing the stress field from the deformation, especially in the scenario such as grasp adjustment after a perturbation, or measuring the compliance of an object. The silicone-based sensor is highly compliant, which is useful for the automatic control of grasping, human-robot interactions and teleoperation. In the case of extremely large displacements, it can happen that the soft markers will be visible between two transparent filters. In this case, the single marker approach will not be appropriate. Since the sensor consists of two regularly spaced grids of markers, a large scale interference similar to the Moiré pattern will be observed. Viewed from afar, the colored fringes produced by the sensor provide information about the shape of the object and the friction forces at work.

Acknowledgment

The authors would like to thank Julien Diperi and Stéphane Viollet for enlightening discussions.

REFERENCES

[1] L. Natale and E. Torres-Jara, "A sensitive approach to grasping," in *Proceedings of the sixth international workshop on epigenetic robotics*, 2006, pp. 87–94.

[2] R. S. Johansson and J. R. Flanagan, "Coding and use of tactile signals from the fingertips in object manipulation tasks," *Nature Reviews Neuroscience*, vol. 10, no. 5, pp. 345–359, 2009.

[3] T. André, V. Lévesque, V. Hayward, P. Lefèvre, and J.-L. Thonnard, "Effect of skin hydration on the dynamics of fingertip gripping contact," *Journal of The Royal Society Interface*, vol. 8, no. 64, pp. 1574–1583, 2011.

[4] B. Delhaye, P. Lefevre, and J.-L. Thonnard, "Dynamics of fingertip contact during the onset of tangential slip," *Journal of The Royal Society Interface*, vol. 11, no. 100, p. 20140698, 2014.

[5] R. S. Dahiya, G. Metta, M. Valle, and G. Sandini, "Tactile sensing—from humans to humanoids," *IEEE transactions on robotics*, vol. 26, no. 1, pp. 1–20, 2010.

[6] M. Strohmayr, H. Wörn, and G. Hirzinger, "The dlr artificial skin step i: Uniting sensitivity and collision tolerance," in *Robotics and Automation (ICRA), 2013 IEEE International Conference on*. IEEE, 2013, pp. 1012–1018.

[7] R. D. Howe and M. R. Cutkosky, "Dynamic tactile sensing: Perception of fine surface features with stress rate sensing," *IEEE transactions on robotics and automation*, vol. 9, no. 2, pp. 140–151, 1993.

[8] B. Li, Y. Shi, A. Fontecchio, and Y. Visell, "Mechanical imaging of soft tissues with a highly compliant tactile sensing array," *IEEE Transactions on Biomedical Engineering*, vol. 65, no. 3, pp. 687–697, 2018.

[9] N. Wettels, V. J. Santos, R. S. Johansson, and G. E. Loeb, "Biomimetic tactile sensor array," *Advanced Robotics*, vol. 22, no. 8, pp. 829–849, 2008.

[10] A. Kadowaki, T. Yoshikai, M. Hayashi, and M. Inaba, "Development of soft sensor exterior embedded with multi-axis deformable tactile sensor system," in *Robot and Human Interactive Communication, 2009. RO-MAN 2009. The 18th IEEE International Symposium on*. IEEE, 2009, pp. 1093–1098.

[11] H. Shinoda, K. Matsumoto, and S. Ando, "Acoustic resonant tensor cell for tactile sensing," in *Robotics and Automation, 1997. Proceedings., 1997 IEEE International Conference on*, vol. 4. IEEE, 1997, pp. 3087–3092.

[12] D. Xu, G. E. Loeb, and J. A. Fishel, "Tactile identification of objects using bayesian exploration," in *Robotics and Automation (ICRA), 2013 IEEE International Conference on*. IEEE, 2013, pp. 3056–3061.

[13] T. Maeno, S. Hiromitsu, and T. Kawai, "Control of grasping force by detecting stick/slip distribution at the curved surface of an elastic finger," in *Robotics and Automation, 2000. Proceedings. ICRA'00. IEEE International Conference on*, vol. 4. IEEE, 2000, pp. 3895–3900.

[14] S. Hirai *et al.*, "A novel model for assessing sliding mechanics and tactile sensation of human-like fingertips during slip action," *Robotics and Autonomous Systems*, vol. 63, pp. 253–267, 2015.

[15] N. J. Ferrier and R. W. Brockett, "Reconstructing the shape of a deformable membrane from image data," *The International Journal of Robotics Research*, vol. 19, no. 9, pp. 795–816, 2000.

[16] B. Ward-Cherrier, N. Pestell, L. Cramphorn, B. Winstone, M. E. Giannaccini, J. Rossiter, and N. F. Lepora, "The tactip family: Soft optical tactile sensors with 3d-printed biomimetic morphologies," *Soft robotics*, vol. 5, no. 2, pp. 216–227, 2018.

[17] K. Sato, K. Kamiyama, N. Kawakami, and S. Tachi, "Finger-shaped gelforce: sensor for measuring surface traction fields for robotic hand," *IEEE Transactions on Haptics*, vol. 3, no. 1, pp. 37–47, 2010.

[18] M. K. Johnson and E. H. Adelson, "Retrographic sensing for the measurement of surface texture and shape," in *Computer Vision and Pattern Recognition, 2009. CVPR 2009. IEEE Conference on*. IEEE, 2009, pp. 1070–1077.

[19] C. Chorley, C. Melhuish, T. Pipe, and J. Rossiter, "Development of a tactile sensor based on biologically inspired edge encoding," in *Advanced Robotics, 2009. ICAR 2009. International Conference on*. IEEE, 2009, pp. 1–6.

[20] K. Kamiyama, K. Vlack, T. Mizota, H. Kajimoto, K. Kawakami, and S. Tachi, "Vision-based sensor for real-time measuring of surface traction fields," *IEEE Computer Graphics and Applications*, vol. 25, no. 1, pp. 68–75, 2005.

[21] F. Guo, C. Zhang, Y. Yan, P. Li, and Z. Wang, "Measurement of three-dimensional deformation and load using vision-based tactile sensor," in *Industrial Electronics (ISIE), 2016 IEEE 25th International Symposium on*. IEEE, 2016, pp. 1252–1257.

[22] R. Li, R. Platt, W. Yuan, A. ten Pas, N. Roscup, M. A. Srinivasan, and E. Adelson, "Localization and manipulation of small parts using gelsight tactile sensing," in *Intelligent Robots and Systems (IROS 2014), 2014 IEEE/RSJ International Conference on*. IEEE, 2014, pp. 3988–3993.

[23] W. Yuan, R. Li, M. A. Srinivasan, and E. H. Adelson, "Measurement of shear and slip with a gelsight tactile sensor," in *Robotics and Automation (ICRA), 2015 IEEE International Conference on*. IEEE, 2015, pp. 304–311.

[24] S. Weinstein, "Intensive and extensive aspects of tactile sensitivity as a function of body part, sex and laterality," *The skin senses*, 1968.

[25] A. Bicchi, "On the closure properties of robotic grasping," *The International Journal of Robotics Research*, vol. 14, no. 4, pp. 319–334, 1995.

[26] M. Wiertlewski, J. Lozada, and V. Hayward, "The spatial spectrum of tangential skin displacement can encode tactual texture," *IEEE Transactions on Robotics*, vol. 27, no. 3, pp. 461–472, 2011.

[27] M. Shimojo, "Mechanical filtering effect of elastic cover for tactile sensor," *IEEE Transactions on Robotics and Automation*, vol. 13, no. 1, pp. 128–132, 1997.

[28] K. L. Johnson and K. L. Johnson, *Contact mechanics*. Cambridge university press, 1987.

[29] T. Maeno, T. Kawamura, and S.-C. Cheng, "Friction estimation by pressing an elastic finger-shaped sensor against a surface," *Robotics and Automation, IEEE Transactions on*, vol. 20, no. 2, pp. 222–228, 2004.

[30] Y. Hu, R. Katragadda, H. Tu, Q. Zheng, Y. Li, and Y. Xu, "Bioinspired 3-d tactile sensor for minimally invasive surgery," *Journal of microelectromechanical systems*, vol. 19, no. 6, pp. 1400–1408, 2010.

[31] A. Yamaguchi and C. G. Atkeson, "Combining finger vision and optical tactile sensing: Reducing and handling errors while cutting vegetables," in *Humanoid Robots (Humanoids), 2016 IEEE-RAS 16th International Conference on*. IEEE, 2016, pp. 1045–1051.

[32] L. Osborn, R. R. Kaliki, A. B. Soares, and N. V. Thakor, "Neuromimetic event-based detection for closed-loop tactile feedback control of upper limb prostheses," *IEEE transactions on haptics*, vol. 9, no. 2, pp. 196–206, 2016.